

# Model-Based Adaptive Precision Control for Tabletop Planar Pushing Under Uncertain Dynamics

Aydin Ahmadi<sup>1</sup> and Baris Akgun<sup>1\*</sup>

<sup>1\*</sup>Computer Engineering Department, Koç University, Rumelifeneri Yolu, Istanbul, 34450, Istanbul, Turkey.

\*Corresponding author(s). E-mail(s): [baakgun@ku.edu.tr](mailto:baakgun@ku.edu.tr);  
Contributing authors: [aahmadi22@ku.edu.tr](mailto:aahmadi22@ku.edu.tr);

## Abstract

Data-driven planar pushing methods have recently gained attention as they reduce manual engineering effort and improve generalization compared to analytical approaches. However, most prior work targets narrow capabilities (e.g., side switching, precision, or single-task training), limiting broader applicability. We present a model-based framework for non-prehensile tabletop pushing that uses a single learned model to address multiple tasks without retraining. Our approach employs a recurrent GRU-based architecture with additional non-linear layers to capture object–environment dynamics while ensuring stability. A tailored state–action representation enables the model to generalize across uncertain dynamics, variable push lengths, and diverse tasks. For control, we integrate the learned dynamics with a sampling-based Model Predictive Path Integral (MPPI) controller, which generates adaptive, task-oriented actions. This framework supports side switching, variable-length pushes, and objectives such as precise positioning, trajectory following, and obstacle avoidance. Training is performed in simulation with domain randomization to support sim-to-real transfer. We first evaluate the architecture through ablation studies, showing improved prediction accuracy and stable rollouts. We then validate the full system in simulation and real-world experiments using a Franka Panda robot with markerless tracking. Results demonstrate high success rates in precise positioning under strict thresholds and strong performance in trajectory tracking and obstacle avoidance. Moreover, multiple tasks are solved simply by changing the controller’s objective function, without retraining. While our current focus is on a single object type, we extend the framework by training on wider push lengths and designing a balanced controller that reduces the number of steps for longer-horizon goals.

**Keywords:** Planar-pushing, Robot learning, Model predictive control, Object manipulation

## 1 Introduction

Pushing, a form of non-prehensile manipulation, lets robots pose objects without the need for grasping, allowing them to perform a variety of tasks. Various approaches have been explored to address this problem through planning, control, and reinforcement learning (Stüber et al., 2020).

Traditional approaches model push dynamics analytically and use a controller and/or a planner to generate actions (Mason, 1986; Goyal et al., 1989; Jia and Erdmann, 1999; Lee et al., 2015). Modeling requires explicit parameters of the objects, such as mass, center of mass (COM) and shape, along with environmental factors like friction and potential disturbances. However,

modeling and controller design require sophisticated engineering. Additionally, they struggle with generalization in real-world scenarios when the objects or environment parameters change, often necessitating fine-tuning of parameters or even re-engineering. Moreover, these parameters are not always available, requiring system identification.

As a response to the limitations of traditional model-based methods, data-driven approaches have emerged to address some of the associated challenges (Bauza and Rodriguez, 2017; Li et al., 2018; Bauza et al., 2019; Kloss et al., 2020; Cong et al., 2020; Gao et al., 2020). These methods are typically based on learning from experience, where a robot interacts with objects to collect data. The data is used to learn dynamics of object pushing which is then coupled with a push controller and/or the robot can use the interactions directly to learn how to push objects. Rather than relying on explicitly specified physical parameters such as mass or friction, some of these approaches handle the inherent uncertainty and variability in real-world interactions by through learning. Methods based on model learning, model-based approaches, aim to approximate the forward dynamics of pushing through supervised learning. In this framework, the robot first collects a dataset of interaction trajectories, often consisting of proprioceptive or visual observations and corresponding object motion outcomes. A predictive model, typically a neural network or a probabilistic regressor, is then trained to map observations and actions to future object states. Once trained, this model is used in conjunction with a controller or planner to compute action sequences that achieve a desired goal (Bauza and Rodriguez, 2017; Li et al., 2018; Bauza et al., 2019; Kloss et al., 2020; Cong et al., 2020; Gao et al., 2020). One major advantage of this model-controller/planner decoupling is modularity: a well-learned dynamics model can be reused across multiple tasks, allowing practitioners to plug in different controllers or planners depending on the specific objective. Moreover, these approaches are capable of learning end-to-end mappings from raw sensory inputs—such as vision or proprioception—to predicted outcomes, effectively bypassing the need for handcrafted features or explicit modeling of object properties. However, learned models are not without their limitations.



**Fig. 1:** The real-robot setup. The robot holds a stick with a small ball at the end to interact with the objects. A RGBD camera is used for perception.

Another subset of data-driven approaches is model-free methods. These approaches aim to directly learn a pushing policy that maps sensory inputs to actions, without explicitly modeling the underlying object dynamics. Given a goal state, the agent learns through trial and error to generate actions that guide the object toward the desired configuration. Once a policy is trained, action inference is extremely fast, requiring only a forward pass through a neural network, making model-free methods attractive for real-time applications. However, these methods require a lot of training hours on top of requiring separate training for each desired task.

We take a model-based approach based on our main motivation of training economy; train a push model once and adapt the controller/planner for multiple tasks. Towards this end, we propose a novel GRU-based architecture for learning push dynamics and use a sampling-based Model Predictive Control (MPC) approach, specifically a modified version of Model Predictive Path Integral (MPPI(Williams et al., 2016)), for planar object manipulation on a table. We design our architecture to implicitly capture, potentially non-stationary, object and environmental dynamics by utilizing a recent set of previous state-action pairs, with an emphasis on the current state-action pair.

Our unique state-action representation includes the previous change of object pose, current object relative robot position (contact position) and the object relative push vector

(both magnitude and direction). Our state-action representation and our choice of sampling-based MPC allows for changing the object sides during pushing. In addition, our sampling approach is goal-aware, which lets us generate different length pushes based on the current goal and adapt the samples for the task at hand. To the best of our knowledge, this is the first model-based approach that employs multi-length pushes. Our approach handles local optima for positioning, allows for additional objectives such as obstacle avoidance or different tasks such as trajectory following, and can trade-off task duration with high-precision. We train our model in simulation and collect different length and direction pushes with domain-randomization (Tobin et al., 2017; Peng et al., 2018) to facilitate sim-to-real transfer. We evaluate our approach both in simulation and on a real-world setup as shown in Fig. 1. The contributions of our work are:

- A robust adaptive model-based framework that supports changes to the controller’s objectives or training dataset, enabling generalization to additional subtasks
- A dataset strategy and a tailored state–action representation that enable sampling from a wide range of pushes, allowing the model to capture rich environment–interaction dynamics while supporting variable push lengths and side-switching for improved accuracy and optimality.
- Detailed evaluations both in simulation and on a real robot setup using Franka Emika Panda robot, demonstrating the effectiveness of our method.

## 2 Related work

Pushing based manipulation can be divided into (i) analytical methods, (ii) model-based data-driven methods, and (iii) model-free data-drive methods. In the first two, models for push dynamics and controllers/planners are used to generate actions. The model is engineered in the first and learned in the second. In the third, a push policy is directly learned.

### 2.1 Analytical methods

(Mason, 1986) develop an analytical model for quasi-static planar pushing. (Goyal et al., 1989) expand this with the limit surface idea, which

defines the relationship between sliding motion of the object and friction under the quasi-static assumption. This is used to determine the object velocity for a given pushing force. (Lynch, 1992) investigate planar pushing using sliding and sticking motions, and employ a search algorithm for planning. (Lee et al., 2015) introduce a hierarchical planning method for generating sequences of non-prehensile actions, where contact points for pushing are derived as part of the planning process. This approach is designed to reduce the overall search space by decomposing the full manipulation task into smaller sub-problems, allowing more efficient planning in complex environments. While analytical approaches offer interpretability and task-specific optimality under idealized conditions, their practical application is constrained by the need for accurate object-specific parameters such as mass, center of mass, and surface friction. These values are often difficult to measure in real-world scenarios, and even small deviations can lead to substantial performance degradation. They also lack generalization and are resource-demanding.

### 2.2 Data-driven model based methods

Data-driven model-based methods aim to reduce engineering effort and better handle uncertainty. (Arruda et al., 2017) use Gaussian Process Regression and an Ensemble of Mixture Density Networks to evaluate uncertainty of object motion predictions. While their method demonstrates the ability to switch object sides during planning, it lacks evaluation in sim-to-real scenarios, limiting its generalizability to novel objects. Additionally, their approach does not support multi-length pushes and does not include planning-based task evaluations. Push-Net. (Li et al., 2018) leverages an LSTM module to encode temporal pushing interactions and incorporates an auxiliary objective to estimate the object’s center of mass, implicitly embedding physical reasoning. The approach uses object-segmented masks as visual input and demonstrates the ability to generalize to novel objects. However, their method uses a relatively coarse goal threshold—5 cm for position and 10° for orientation—and employs a fixed push length of 2.5 cm, resulting in a success rate lower than ours.

(Yu et al., 2016; Bauza and Rodriguez, 2017; Bauza et al., 2019) demonstrate the effectiveness of learning models based on collected data that include shape, friction, mass distribution, and perceptual information. (Yu et al., 2016) present a large-scale dataset of planar pushing interactions, comprising over one million samples that include both positional data of the pusher and object, as well as corresponding interaction forces. (Bauza and Rodriguez, 2017) used a Gaussian process-based model to predict both the outcome and variability of planar pushing, incorporating pusher velocity to relax the quasi-static assumption. While effective, the approach lacks generalization to novel objects, does not employ domain randomization, and focuses solely on model learning without addressing the control aspect. More recently, (Bauza et al., 2019) presents a large dataset containing object pose information and visual data (RGB-D), and also introduces models trained on this dataset. However, their approach struggles with precise control of cubic objects, as it selects push points randomly within a 9–10 cm range and uses a fixed push length of 5 cm—limitations reflected in their reported results. (Kloss et al., 2020) introduce a hybrid model that integrates deep learning and analytical physics to predict planar object motion using RGB-D data. Their method estimates object pose and friction parameters through an analytical filter and learns an affordance model via CNNs. It uses object masks to classify motion outcomes, blending perception with physical modeling. While it requires no prior object knowledge, its property estimations are limited and error-prone, and it relies on assumptions of uniform properties and known friction, which limits generalization.

There are model-based methods that do not rely on object-environment parameters. (Cong et al., 2020) propose a model-based strategy using a recurrent model and sampling-based MPC for control, which is similar to our approach. However, their approach ignores object orientation control, suffers from high sampling costs, does not consider multi-length pushes, and they do not include additional tasks. Other drawbacks of their method include the fact that the direction and pose of the first actions did not affect the action selection for the next step. Additionally, it exhibited a low success rate within the

threshold of 2.5 cm. (Gao et al., 2020) introduce a few-shot learning approach for predicting the motion of objects with varying shapes. While their method demonstrates promising results for translation prediction, it overlooks critical factors such as object orientation and the historical trajectory of object motion—both of which are essential for achieving smooth and reliable rearrangement. In contrast, our model addresses these limitations by incorporating both historical actions and environmental dynamics, enabling accurate predictions of object motion in terms of both position and orientation. Furthermore, our predictions demonstrate higher accuracy compared to the statistical performance reported in their work.

More recently, (Wang et al., 2024) proposed an online framework for trajectory-following tasks by leveraging a non-parametric model, showing promising results for both model learning and control. However, their reliance on non-parametric methods for online learning in real-world settings makes the approach time-consuming and prone to errors, whereas our system—trained with domain randomization in simulation—requires less than three hours from data collection to controller deployment. Moreover, our framework offers greater adaptability in pushing strategies and supports obstacle avoidance, while their perturbed inverse dynamics trajectories do not accommodate obstacle avoidance. In contrast, our data-driven approach not only avoids the need for retraining across different configurations but is also equipped with a system capable of effectively handling obstacle avoidance.

### 2.3 Model-free methods

Model-free reinforcement learning (RL) based methods overcome the online scalability challenges of MPC, at the expense of extensive training. (Cong et al., 2022) employ an RL method incorporating visuo-proprioception for objects of various shapes in planar pushing tasks. However, their performance is lacking and they do not incorporate the orientation of target as their objective. (Wang et al., 2023) propose a model-free RL method that uses contact force in their rewards. They only use a positioning task even though they utilize object and end-effector orientations. (Ferlandis et al., 2023) introduce a RL-based method

for pushing cubic objects, using categorical exploration.

While their method shows promising results, there are several drawbacks. The required amount of transitions for proper training are in the order of billions. Since they use global coordinates for observations, their operational table size and target location are limited. A later version (Dengler et al., 2024) handles object collisions, however, as with any model-free method, the policies must be retrained for each task.

## 3 Methodology

### 3.1 Push Dynamics Model

#### 3.1.1 Architecture

We introduce and evaluate our push dynamics model in this section. Our model takes object-robot configuration and robot action related inputs, without any explicit object-environment physical parameters, and predicts the change of object pose. We use a history of state-action pairs and Gated Recurrent Unit (GRU) layers to infer implicit dynamics while emphasizing the most recent pair for accuracy. The inputs to the model consist of the history of the previous state-action pairs. We take the object orientation into account in addition to the position. However, the pusher is only represented with a position since we assume a single contact point. Let  $t$  be the current time step,  $O_t$  denote the object pose in the plane (2D translation and orientation about the  $z$ -axis) and  $R_t$  be the 2D pusher position at  $t$ . Then, a single pair includes object motion of the previous time step ( $\Delta O_t = O_{t-1}^{-1}O_t$ ), the relative position of the pusher with respect to the object ( $RO_t = O_t^{-1}R_t$ ), and the current relative pusher motion ( $\Delta RO_t = R_{t+1} - R_t$ ), indicating the direction and magnitude of the push. These are depicted geometrically in Fig. 3. Then current input is the history from time step  $t - w + 1$  to  $t$  (where  $w$  denotes the window length), represented as:

$$H_t = \{(\Delta O_k, RO_k, \Delta RO_k)\}_{k=t-w+1}^t \quad (1)$$

Our model, denoted as  $f$ , takes the history as input and outputs the predicted object motion for

the next time-step:  $\Delta \hat{O}_{t+1} = f(H_t)$ . The architecture of our model can be seen in Fig. 2. From the perspective of the model, the action part is the location, direction and magnitude of the push ( $RO_t, \Delta RO_t$ ) and the previous pushes are part of the history. As such, we emphasize this in our model along with the latest object motion which holds the latest object-environment interaction information.

These are separately given to a fully-connected (FC) layer. In parallel, the historical part from  $t - w + 1$  to  $t - 1$  is input to a GRU layer. The output of this layer encodes the object and environment properties along with pusher-object interactions. The FC and GRU output dimensions are the same to avoid one of them dominating the other. These outputs are concatenated and passed through 2 FC layers before the output layer. All FC layers have ReLU activations.

#### 3.1.2 Data Collection

We collect training data through random pushing interactions in a simulated environment using PyBullet, building upon the framework provided by (Ferrandis et al., 2023). A total of 10,000 episodes are recorded, each consisting of 100 pushes applied to a planar cubic object with randomized parameters. To ensure diversity in object poses and avoid bias in the training distribution, we incrementally rotate the object by one degree across episodes. The pushing magnitudes range from 2 mm to 3 cm, and push directions are sampled uniformly within a symmetric cone of angle  $\pi/4$  oriented towards the object at the point of contact. This setup ensures a broad distribution of contact angles and motion outcomes. The pushes are applied from points sampled on the perimeter of a square surrounding the object, with a margin of 1 cm beyond its actual size, assuming the  $z$ -axis remains fixed. Figure 4 illustrates a sample pushing configuration from the dataset. To enhance the generalization of our learned model and promote sim-to-real transferability, we employ domain randomization during data collection. Following the principles established in (Tobin et al., 2017; Peng et al., 2018), we randomly vary several environmental and object parameters at the beginning of each episode. These parameters include the object’s mass, dimensions, friction coefficient, and

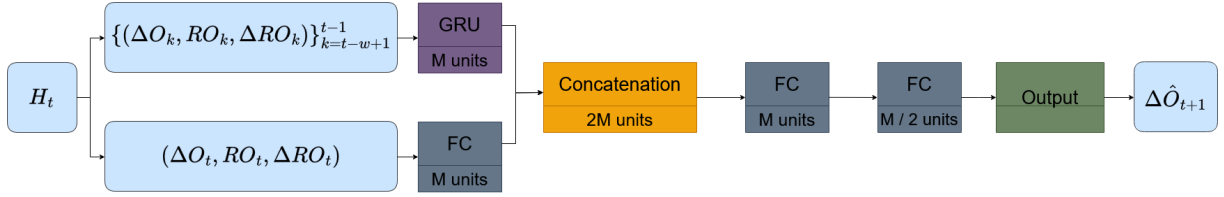


**Fig. 2:** Push dynamics model architecture. The  $(RO_t, \Delta RO_t)$  parts of the input constitute the action.

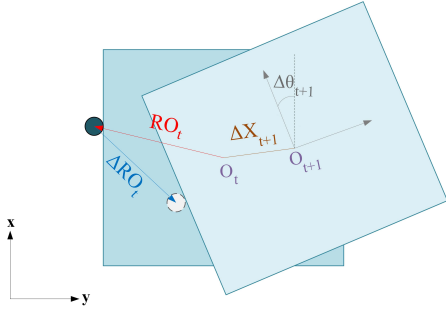


**Fig. 3:** State-action representation.  $O_t$  represents the 2D object pose before the push and  $O_{t+1}$  represents it after the push.  $RO_t$  represents the position of the pusher with respect to object before the push and  $\Delta RO_t$  represents the pusher motion.  $\Delta X_{t+1}$  and  $\Delta \theta_{t+1}$  denote the changes in the object’s position and orientation, respectively, after the push, and  $\Delta O_{t+1} = (\Delta X_{t+1}, \Delta \theta_{t+1})$ .

the restitution of the supporting surface. The exact ranges and details of these parameters are listed in Table 1. This strategy enables the model to learn robust contact dynamics across a wide variety of scenarios, reducing overfitting to a narrow domain. Notably, we observed that the model trained entirely on simulated data generalized effectively to real-world robot experiments without requiring any additional fine-tuning. This highlights the effectiveness of combining fully random pushing actions with domain randomization for robust and scalable data-driven manipulation learning. For the improved version of our framework, which we discuss later in Section 3.2, we sample pushing magnitudes between 3mm and 5cm.

### 3.1.3 Training

We use two models in practice: one for predicting the 2D translational motion and another for

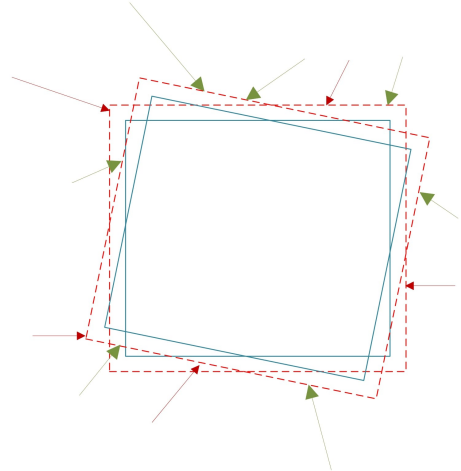


**Fig. 4:** Data collection process. This figure illustrates the data collection process over 10,000 episodes. Actions are sampled with directions uniformly distributed between  $-45^\circ$  and  $45^\circ$ , and push magnitudes ranging from 2 mm to 3 cm. The red dots indicate the boundary of relative poses where actions are applied, designed to prevent premature contact (i.e., touching) before the action is executed.

predicting the rotational motion about the plane-normal. The loss for the translation prediction model is defined as the mean squared distance between the target and the predicted translations. The loss for the orientation prediction model is defined as the mean non-oriented angular difference between the target and the predicted rotations. The non-oriented angle is calculated as follows:

$$D_\theta(\theta_1, \theta_2) = \min(|\theta_1 - \theta_2|, 2\pi - |\theta_1 - \theta_2|) \quad (2)$$

Two models performed better in practice, mainly due to removing the need for tuning the

**Table 1:** Domain randomization parameters

Parameter	Sampling Distribution
Friction	[0.5, 0.7]
Restitution	[0.4, 0.6]
Object Length	[0.11, 0.13] m
Object Width	[0.09, 0.11] m
Object Mass	[0.3, 0.7] kg

relative weights of the position and the orientation losses. These models use the exact same architecture other than the output size and we use  $M = 64$  (see Fig. 2) to instantiate both of them. We perform a 0.7-0.2-0.1 train-validation-test set splits. The models were trained using the Adam optimizer (Kingma and Ba, 2014) with a learning rate scheduler. A total of 40 epochs were enough for convergence in all cases and we take the model with the best validation performance.

### 3.1.4 Model Evaluation

We evaluated our model on one-step predictions from the test set. We pick two baselines to demonstrate the effectiveness utilizing the history while focusing on the current time-step in our architecture. The first baseline is the 2-layer LSTM model proposed in (Cong et al., 2020), which we use directly with the same number of hidden units as in our model. The second baseline is a model that does not incorporate history.

Table 2 presents the prediction performance of these three models and the model for the improved version. We further divided the test set into two sets to capture the performance of the models with different length pushes. The "big" set contains pushes from 8 mm to 3 cm, while the "small" set contains pushes from 2 mm to 8 mm. For the improved version the pushes are from 3mm to 5cm.

Our model outperforms both of the baselines. The performance compared to the no history baseline is expected. The no history model cannot infer the object properties with just looking at the current state. On the other hand, the first baseline performed the worst - particularly bad for position prediction - even though it was taking the history into account. Overfitting is the main culprit. The best model had good training and validation performances. One additional potential reason is

that the action cannot influence the prediction enough and it gets dwarfed by the history. Since our dataset is heavily randomized, this particular architecture (limited inductive bias compared to ours) arguably did not have enough data points to generalize. As such, we conclude that our architecture provides a good balance between historical information to infer pushing properties and the current action to perform accurate predictions. Furthermore, the time for each step prediction is 2 ms.

## 3.2 Control

We use a modified MPPI as our controller which is a sampling-based method for efficiently generating actions. The basic idea is to sample a number of actions, predict corresponding rollouts using a model, calculate their objective value (e.g. cost, reward), calculate the next action based on these, apply the first action, then repeat. Note that the objective values are defined for a given task and we assume they are to be minimized. For example, distance of the last position of a rollout to the target can be an objective function for positioning. The single time-step of this control method is depicted in Alg. 1.

We use a goal-aware sampling procedure. In our initial approach, the relative pusher position ( $RO$ ) and the push magnitude were sampled simultaneously from the dataset. For a single sample, a random location on the periphery of the object ( $RO$ ) is picked, followed by a random push direction within a symmetric  $\pi/4$  cone towards the object. We then randomly pick a push length but the range is selected based on the goal. The direction and length is used to calculate  $\Delta RO$ . The object dimensions ( $D_O$ ) are required for some these steps. This approach allows us to switch object sides and perform different length pushes. We use  $a_i = [RO^i, \Delta RO^i]$  to represent the  $i^{th}$  sampled action as a 4 dimensional vector.

In a single control step, we sample  $N$  actions (line 4) and generate  $N$  rollouts by applying each sampled action repeatedly for a fixed horizon length,  $T$ . We use the model ( $f(\cdot)$ ) in an autoregressive way to generate an individual rollout (line 5) and denote the  $i^{th}$  rollout as  $\tau_i$ . Then the objective values ( $c_i$ ) of the rollouts are calculated (line 5), based on the given objective function  $c(\tau)$ . The action selection is done by taking the weighted

**Table 2:** Object motion prediction performance of our proposed model and baselines. Positions are in millimeters and orientations are in radians. The values in parenthesis denote the standard deviations. The **Avg. Position Err** values (with parentheses) denote the mean error in millimeters and their standard deviations. The **Avg. Orientation Err** values (with parentheses) denote the mean error in radians and their standard deviations. The last row shows the results for the improved version model.

Model / Set	Avg. Position Err.	Avg. Orientation Err.
No History - Small Set	0.6 (0.4)	0.004 (0.004)
(Cong et al., 2020) - Small Set	1.2 (0.6)	0.016 (0.012)
Ours - Small Set	<b>0.3 (0.3)</b>	<b>0.003 (0.003)</b>
No History - Big Set	1 (1)	0.01 (0.015)
(Cong et al., 2020) - Big Set	6.2 (3.6)	0.077 (0.052)
Ours - Big Set	<b>0.8 (0.8)</b>	<b>0.007 (0.009)</b>
New model for improved version of controller	1.5 (1.7)	0.016 (0.023)

---

**Algorithm 1** Action Selection in our MPPI implementation

---

- 1: **Fixed Input:**  $D_O, N, T, c(\cdot), f(\cdot), \lambda$
  - 2: **Input:** The state-action history of the previous  $w - 1$  steps and latest object motion  $\Delta O_t$  ( $\bar{H}_t$ ), the current object pose  $O_t$
  - 3: **Output:** The next action ( $RO_t, \Delta RO_t$ ) and the predicted object motion ( $\Delta \hat{O}_{t+1}$ )
  - 4:  $A = a_1, a_2, \dots, a_N \leftarrow \text{sampleActions}(D_O, O_t, N)$
  - 5:  $\tau = \tau_1, \tau_2, \dots, \tau_N \leftarrow \text{generateRollouts}(f, A, T, \bar{H}_t)$
  - 6:  $C = c_1, c_2, \dots, c_N \leftarrow \text{calculateObjectiveValues}(c, \tau)$
  - 7:  $\Omega = \omega_1, \omega_2, \dots, \omega_N \leftarrow \text{calculateActionWeights}(C)$  (Eq. 3)
  - 8:  $a_t \leftarrow \text{combineActions}(A, \Omega)$  (Eq. 4)
  - 9:  $\Delta \hat{O}_{t+1} \leftarrow f(H_t)$ , ( $H_t$  includes  $a_t$ )
  - 10: **return**  $a_t, \Delta \hat{O}_{t+1}$
- 

combination of the sampled actions. Individual action weights are calculated with the Eq. 3. Then, the actions are combined using the Eq. 4 where  $a_t = [RO_t, \Delta RO_t]$  is the selected action. These steps are in (line 7-8).

$$\omega_i = \frac{\exp\left(\frac{-c_i}{\lambda}\right)}{\sum_{j=1}^N \exp\left(\frac{-c_j}{\lambda}\right)} \quad (3)$$

$$a_t = \frac{\sum_{i=1}^N (\omega_i \times a_i)}{\sum_{i=1}^N \omega_i} \quad (4)$$

This approach prioritizes actions that are more effective in reducing the objective value (e.g. distance) while still allowing other actions to affect the outcome to avoid being overly greedy. The trade-off is set by the parameter  $\lambda$ . However, the

resulting relative pusher position may be in collision with the object. In that case, we restart the sampling process. If we cannot find a feasible solution in 20 restarts, we select the action with the lowest cost.

The next step is to apply the action (not shown in the algorithm). The robot end-effector pose is calculated based on the current object pose  $O_t$  and the selected relative pusher position  $RO_t$ . We use a motion-planner to reach this pose. Then, the robot is moved based on the selected  $\Delta RO_t$ , using a Cartesian controller. After the robot motion, the object pose is recalculated using an external camera. This process repeats until an objective (e.g., object within a threshold) or a maximum number of iterations are reached.

For basic method, we adopt a two-stage control approach. In the first stage, the primary aim is to rapidly bring the object close to the target which is achieved by sampling longer pushes. We switch to the second stage once the object is within 1 cm of the object. In the second stage, the strategy changes to sampling shorter pushes. The idea is to perform precise adjustments and accurately pose the object. In the first stage, the pushes are sampled in the range 8mm-3cm, and in the second stage, from 1 mm to 8 mm.

To improve the performance and robustness of this method, we introduce several modifications aimed at enhancing both the diversity of sampled actions and the precision of the action selection process. First, we increase the number of sampled actions per control iteration, enabling a denser exploration of the action space and significantly increasing the likelihood of identifying high-quality actions. Instead of sampling  $RO_t$  and

$\Delta RO_t$  jointly, we now sample each component separately. A balanced number of  $RO_t$  values are sampled from all four sides of the cube, which encourages more diverse and symmetric interaction strategies. We also expand the sampling range of push magnitudes to span from 3 mm to 5 cm, thereby accommodating both coarse repositioning and fine-tuning within a unified framework.

Another key enhancement concerns the temporal structure of actions during the rollout. Rather than applying the same action across all steps in a rollout, we introduce directional variation at each step. Specifically, while the push magnitude remains constant, the direction changes within a range of  $\pm 5^\circ$  relative to the previous direction. The first action’s direction in the rollout is sampled either from a narrow interval ( $[-5^\circ, 5^\circ]$ ) for more direct pushes, or from a wider interval ( $[-45^\circ, 45^\circ]$ ) for more deviated pushes toward the object. Subsequent actions are then perturbed based on this initial value. This change allows the controller to explore more realistic and continuous action trajectories.

Finally, instead of selecting the action based on a weighted average over sampled rollouts, we adopt a more decisive strategy by directly choosing the action with the minimum rollout cost. This avoids the dilution effect of averaging, which previously led to  $RO_t$  values occasionally falling inside the object boundary. These modifications retain the overall structure of the controller while significantly improving sample efficiency, control accuracy, and robustness across a wide range of pushing scenarios. Algorithm 2 reflects the improved version of our action selection strategy, incorporating enhancements in sampling, rollout generation, and action selection.

### 3.3 Tasks

In our evaluations, we use precise posing of an object as our main task. The aim is to push the object to a target pose (position and orientation). We additionally use two minor tasks; (i) trajectory following and (ii) obstacle avoidance. Trajectory following involves pushing the object along a series of waypoints. Obstacle avoidance, requires the system to reach a target pose while circumventing obstacles that may be on the direct path between the initial and target poses. Each task has its own objective function.

---

#### Algorithm 2 Improved Action Selection in our MPPI Implementation

---

- 1: **Fixed Input:**  $D_O, N, T, c(\cdot), f(\cdot)$
  - 2: **Input:** State-action history  $\bar{H}_t$  of previous  $w-1$  steps, current object pose  $O_t$ , latest object motion  $\Delta O_t$
  - 3: **Output:** Next action ( $RO_t, \Delta RO_t$ ) and predicted object motion  $\Delta \hat{O}_{t+1}$
  - 4:  $RO \leftarrow \text{sampleBalancedROsides}(O_t, N) \triangleright$  Sample  $RO_t$  from all sides of object
  - 5:  $\Delta RO \leftarrow \text{samplePushMagnitudesAndDirections}(N) \triangleright$  Magnitudes in [3 mm, 5 cm], varied directions
  - 6:  $A = a_1, a_2, \dots, a_N \leftarrow \text{combineActions}(RO, \Delta RO)$
  - 7:  $\tau_1, \dots, \tau_N \leftarrow \text{generateDirectionalRollouts}(f, A, T, \bar{H}_t) \triangleright$  Initial direction sampled from  $[-5^\circ, 5^\circ]$  (direct) or  $[-45^\circ, 45^\circ]$  (deviated); subsequent steps perturbed within  $\pm 5^\circ$
  - 8:  $C = c_1, c_2, \dots, c_N \leftarrow \text{calculateObjectiveValues}(c, \tau)$
  - 9:  $i^* \leftarrow \arg \min_i c_i$
  - 10:  $a_t \leftarrow a_{i^*}$
  - 11:  $\Delta \hat{O}_{t+1} \leftarrow f(H_t) \triangleright H_t$  includes  $a_t$
- return**  $a_t, \Delta \hat{O}_{t+1}$
- 

We define the pose difference in Eq. 5, where  $P_i = [X_i, \theta_i]$  is the object pose,  $X_i$  is the associated 2D position vector,  $\theta_i$  is the associated orientation around the 2D plane normal,  $D_\theta$  is from Eq. 2, and  $w_\theta$  is the orientation weight.

$$D_{pose}(P_1, P_2) = \|X_1 - X_2\|^2 + w_\theta D_\theta(\theta_1, \theta_2)^2 \quad (5)$$

**Precise Posing:** In this task, we define the objective function of a rollout as the pose difference between the predicted object pose of the last rollout time step and the target pose, as defined in Eq. 6, where  $\hat{P}_{\text{last}}$  is the predicted object pose at the last rollout time step.

$$c_{\text{posing}}(\tau_i) = D_{pose}(P_{\text{target}}, \hat{P}_{\text{last}}^i) \quad (6)$$

We have an alternative formulation which penalizes the robot travel between pushes, to prevent frequent side-switching for small gains. This is given in Eq. 7, where  $\phi$  is the motion planning penalty weight,  $R_{\text{current}}$  is the last pusher position

and  $R_{\text{sampled}}$  is the sampled pusher position.

$$c_{\text{penalty}}(\tau_i) = c_{\text{posing}}(\tau_i) + \phi \|R_{\text{current}} - R_{\text{sampled}}\|^2 \quad (7)$$

**Trajectory Following:** Trajectory following tasks can have a variety of objective functions. Trajectory following tasks can be formulated using a variety of objective functions, depending on how the trajectory is represented. In our case, we adopt a dense trajectory representation, meaning that waypoints are placed closely along the desired path of the object. Since we repeat the same push during rollouts, it is enough for us to look only at the first step. We also do not expect frequent side-switching due to dense waypoints. As such, we use the simple objective defined in Eq. 8, where  $P_p$  is the next waypoint and  $\hat{P}_{\text{first}}^i$  is the predicted object pose at the first rollout time step.

$$c_{\text{tf}}(\tau_i) = D_{\text{pose}}(P_p, \hat{P}_{\text{first}}^i) \quad (8)$$

**Obstacle Avoidance:** This task is similar to precise positioning with the added requirement of avoiding obstacles. There are multiple objective functions in the literature. We chose a function that exponentially penalizes the distance between the object and the obstacles and the distance between the pusher and the object as defined in Eq. 9, where  $d_o/d_p$  represents the closest distance between the predicted object surface/pusher position during the rollout steps and the closest obstacle surface.

$$c_{\text{oa}} = w_1 \exp(-\alpha_o d_o) + w_2 \exp(-\alpha_p d_p) \quad (9)$$

Here,  $w_1$  and  $w_2$  are weighting factors that determine the relative importance of penalizing proximity between the object and the obstacles ( $w_1$ ) and between the pusher and the object ( $w_2$ ). The parameters  $\alpha_o$  and  $\alpha_p$  control the sensitivity of the exponential penalty to the distances  $d_o$  and  $d_p$ , respectively. In our experiments,  $w_1 = 10$ ,  $w_2 = 10$ , and  $\alpha_o = \alpha_p = 100 \ln(10)$ . During this task, the obstacle avoidance objective is added to the positioning objective only if  $d_o$  or  $d_p$  is less than 1 cm. This formulation penalizes actions that bring the object or the pusher closer than 1 cm to any obstacle, encouraging the selection of safer paths while still making progress towards the target.

This function penalizes actions that bring the object or the pusher closer than 1 cm to any obstacle, encouraging the selection of safer paths that still make progress towards the target.

## 4 Experiments and Results

### 4.1 Simulation

We use the same PyBullet simulation environment to collect model data to evaluate our approach, as illustrated in Fig. 5. The environment consists of a cubic object to be pushed toward a specified goal pose using a spherical pusher of radius 1.25 cm. The horizon length,  $T$ , for precise posing and obstacle avoidance is 5, and it is 1 for trajectory following. The number of samples,  $N$ , is 20 per control step for precise posing and 100 for the other tasks. The orientation weight,  $w_\theta$ , is 0.025 for precise posing, 0 for trajectory following, and 0.3 for obstacle avoidance when the object is within 5 cm of the target pose and 0 elsewhere. The motion planning weight  $\phi$  is dynamic and is the quarter of the distance to the target position in the precise posing task until the object is within 2 cm of the target, at which point it becomes zero. For obstacle avoidance, the robot weight remains zero but for trajectory following we both tested zero and 0.01 weights. In the improved version of our controller, we introduce several key modifications. For precision positioning, we also use a rollout horizon of  $T = 3$  and sample  $N = 100$  actions, distributing them equally across all four sides of the object (25 samples per side).

For benchmarking purposes, we adopt the model-free policy introduced by (Ferrandis et al., 2023) as a baseline for the precise posing task. Specifically, we use the policy trained and released by the original authors without further fine-tuning. This policy was developed using reinforcement learning in simulation and is designed to directly control the pusher to move the object to a desired pose. The observation space for this model-free policy includes both the current pose of the object and the pose of the pusher, providing the agent with sufficient spatial context to infer appropriate actions. The action space consists of velocity commands for the pusher in the 2D plane, allowing for continuous control over its motion.

In addition to this baseline, we evaluate both of our proposed precise posing objectives—based

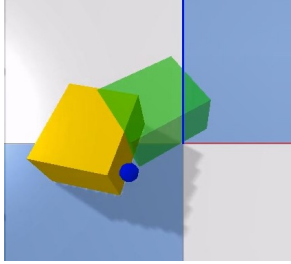


**Fig. 5:** Simulation environment. The figure shows an episode of the precision positioning task, where the object must be pushed to its goal pose using the pusher. In the simulation, the yellowish cube represents the current object pose, the greenish marker indicates the target pose, and the blue sphere represents the pusher.

on Eq. 6 and Eq. 7—within our model-based control framework. These objectives are designed to explicitly guide the pushing behavior by incorporating goal pose alignment and, optionally, penalizing excessive pusher movement.

Beyond precise posing, we also apply our approach to other manipulation tasks, including obstacle avoidance and trajectory following. This broader evaluation demonstrates the generalizability and robustness of our model-based method across diverse pushing scenarios, where each task imposes different constraints on the controller and relies on distinct cost formulations.

**Precise Manipulation:** There are six categories of experiments, each comprising 10 cases. The experiments are organized into two primary categories based on the distance between the initial pose and the target pose. The first category involves target distances ranging from 5 cm to 15 cm, and the second category from 15 cm to 20 cm. Within each distance category, the experiments are further subdivided based on the the target and the initial orientation differences into three intervals:  $0^\circ$ – $30^\circ$ ,  $30^\circ$ – $60^\circ$ , and  $60^\circ$ – $90^\circ$ . Each individual experiment was repeated 5 times, for a total of  $2 \times 3 \times 10 \times 5 = 300$  episodes.

The main results are shown in Fig. 6. The trends within each objective are expected. The number of required steps increase with threshold strictness, with target distance and with orientation difference. However, the model performance did not vary much between the ( $0^\circ$ – $30^\circ$ ) and

( $30^\circ$ – $60^\circ$ ) orientation difference categories. Overall, fewer than 20 steps are required for the object to reach within 1 cm of the target pose. These results also demonstrate the advantage of decoupling the learned model from the controller: greater precision can be achieved simply by allowing more time, without necessitating retraining or altering the policy structure. Although a direct comparison with existing methods is challenging due to variations in evaluation setups and implementation details, our method achieves a favorable trade-off between efficiency and accuracy. It consistently requires fewer steps while maintaining high success rates under stringent error thresholds, attributable to the robustness of the learned dynamics and our approach to generating variable-length push actions.

Including the robot motion penalty increased the required steps as expected, since not switching sides may prolong posing. Fig. 7 demonstrates that incorporating the motion planning cost reduces the robot travel which suggests that trading off number of steps with robot travel is feasible. The average time to finish the pushing episodes is 5.96 seconds.

We evaluated the improved controller on the same six categories described above, as well as on an additional set of experiments involving larger target distances. Specifically, the new set consists of two distance ranges: 10–20 cm and 20–30 cm. Each distance range is further subdivided into three orientation intervals:  $0^\circ$ – $30^\circ$ ,  $30^\circ$ – $60^\circ$ , and  $60^\circ$ – $90^\circ$ , resulting in six new categories. For all categories, we tested two sampling strategies for the initial push direction: a narrow range of  $[-5^\circ, 5^\circ]$  and a wide range of  $[-45^\circ, 45^\circ]$ . The results, presented in Figure 8 and Figure 9, show that the number of steps required to reach each success threshold is reduced by approximately half. Furthermore, Figure 10 illustrates the substantial reduction in robot travel distance achieved by the improved controller. We conducted experiments with horizons of 3 and 4. A smaller horizon may increase the number of steps, but in our case horizon 3 is more suitable since the target is not far for pushes of up to 5 cm per step considering the rollout length. On average, the episode completion time was 5.80 seconds for horizon 3.

We have also compared our method with a model-free baseline. We show the aggregate results

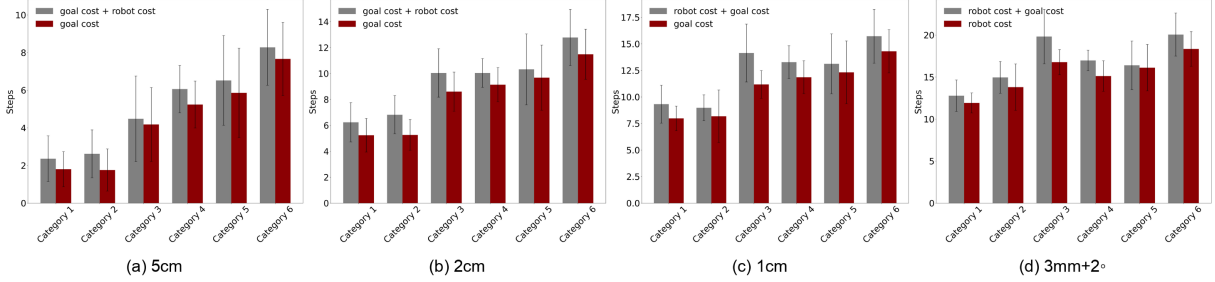


**Fig. 6:** Number of steps taken by the basic method across different categories. The subfigures correspond to different success thresholds: 5 cm, 2 cm, 1 cm, and 3 mm + 2 degrees from left to right. The vertical axes show the steps to reach these thresholds in simulation. The categories in the horizontal axes correspond to the Cartesian product of  $\{(5\text{cm} - 15\text{cm}), (15\text{cm} - 20\text{cm})\}$  (5cm-15cm), (15cm-20cm) distances and  $\{(0^\circ - 30^\circ), (30^\circ - 60^\circ), (60^\circ - 90^\circ)\}$  orientation differences between the initial pose and the target pose (e.g. Category 1 is (5cm-15cm) and  $(0^\circ - 30^\circ)$ , 6 is (15cm-20cm) and  $(60^\circ - 90^\circ)$ ). The crimson and gray bars correspond to the objective functions defined in Eq. 6 and Eq. 7 respectively.

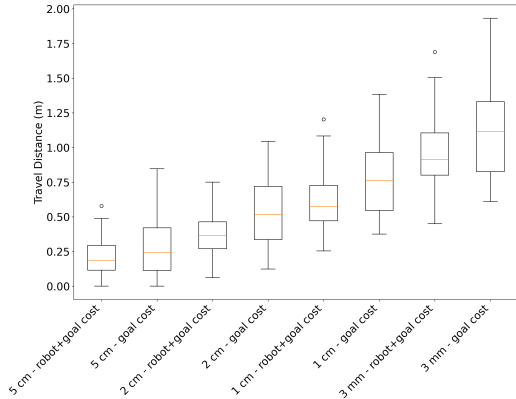


**Fig. 7:** The robot travel for our basic method. The "goal cost" corresponds to Eq. 6 and "robot cost + goal cost" corresponds to Eq. 7. The figure illustrates that pushing the object toward a distant goal with larger orientation changes results in increased robot travel.

in Table 3. Our method achieves 100% task completion rate for both of the thresholds. However, the model-free method performs poorly in addition to the sharp decline between. It can be argued that this baseline would also perform similarly given more training time. However, at some point, training becomes infeasible which is due to the nature of model-free methods. This demonstrates that for certain problems, model-based methods provide more flexibility. In fact, with extended operation (removing stopping thresholds) and careful hyperparameter tuning, we can

**Table 3:** Comparison of Our Method and Model-Free Baseline (Ferrandis et al., 2023).

Threshold	Our Method	Model-Free Baseline
3 mm, $2^\circ$	1.000	0.303
7.5 mm, $5^\circ$	1.000	0.886

achieve errors as low as 1 mm and  $1^\circ$  but the required steps make systematic evaluation difficult.

Lastly, we log the object pose predictions during our experiments. The average error between the model prediction and the object pose after taking the selected action was  $1 \pm 0.84$  mm for distance and  $0.0075 \pm 0.0082$  radians for orientation, similar to the "big set" model evaluation results for our basic method.

**Trajectory Following:** We conduct experiments using both circular and "L"-shaped trajectories composed of dense waypoints. Our controller uses Eq. 8 and performs single-step rollouts to decide the next action. Waypoints are switched once the object reaches sufficiently close proximity to the current target. We tested circular trajectories with radii of 10 cm, 20 cm, and 30 cm, and "L"-shaped paths with side lengths of 10 cm, 20 cm, and 30 cm. For each shape and size, we evaluated two cases: one with no orientation objective and one with a small orientation cost of 0.01. The average position error between the desired and predicted trajectories for following the circular shape ranged

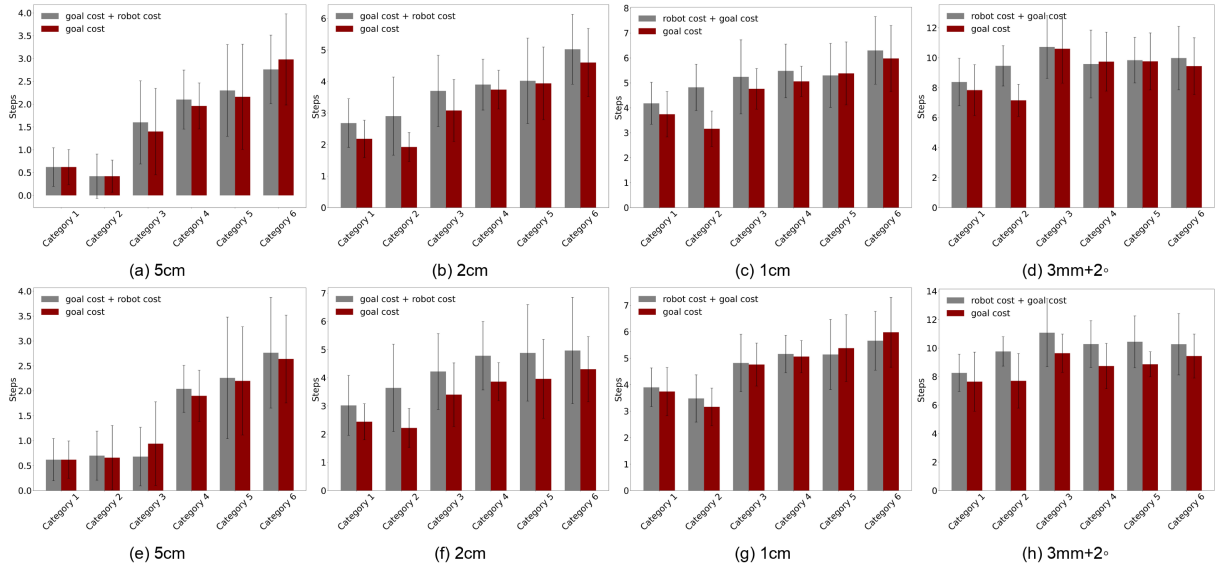


**Fig. 8:** Number of steps taken by the improved method across different categories in short-distance pushing scenarios. Results are evaluated at four success thresholds—5 cm, 2 cm, 1 cm, and 3 mm + 2°—shown from left to right in each group. Each subfigure reports the number of simulation steps required to reach the specified threshold. Rows correspond to different combinations of rollout horizon and initial push direction range: **Row 1** uses Horizon 3 with wide orientation sampling  $[-45^\circ, 45^\circ]$ ; **Row 2** uses Horizon 3 with narrow orientation sampling  $[-5^\circ, 5^\circ]$ . The horizontal axis within each plot categorizes the tasks based on the Cartesian product of translation distance intervals  $\{(5\text{ cm}–15\text{ cm}), (15\text{ cm}–20\text{ cm})\}$  and orientation differences  $\{(0^\circ–30^\circ), (30^\circ–60^\circ), (60^\circ–90^\circ)\}$ . For example, Category 1 denotes 5–15 cm distance and  $0^\circ–30^\circ$  rotation, while Category 6 denotes 15–20 cm and  $60^\circ–90^\circ$ .

from 3 to 4 mm, while for the "L"-shaped trajectory, the average error was between 2 and 3 mm, with the average push length between 1.5 cm and 2 cm. These results highlight how the system's performance varies with different spatial separations between consecutive waypoints. Fig. 11 illustrates representative examples of trajectory following performance in simulation.

**Obstacle Avoidance:** As mentioned before, this task is precise posing with an additional obstacle avoidance term, as defined in Eq. 9. We use the objective function defined in Eq. 6 for posing so that the motion planning cost does not implicitly help obstacle avoidance with less side switching. We use rectangular-prism objects of height 7cm and square base of 3cm and 5cm to simulate obstacles in the environment and evaluate our method under various obstacle configurations from single to multiple obstacles. We ensure each configuration has a collision-free path and repeat them 5 times. Certain configurations require large orientation changes to traverse narrow passages. For

instance, Our method was not successful where the object was required to turn above 60 degrees to get through the passage.

Configurations with single objects or two objects with relatively wide separation are typically easy to handle for the method. As the separation between obstacles decreases, the success rate drops. Additionally, the success rate decreases with the number of obstacles, as expected. Our approach struggles in scenarios requiring the object to rotate significantly—more than  $60^\circ$ —to pass through narrow gaps between two closely placed obstacles. These larger rotation demands highlight the need for more advanced planning capabilities, as the current system's limited planning horizon and fixed action sequences restrict its ability to adapt to complex, intricate maneuvers.

Due to the local nature of the MPC framework, the proposed obstacle avoidance method is not complete. For example, certain cul-de-sac configurations lead to inevitable failures because the controller lacks global re-planning capability.

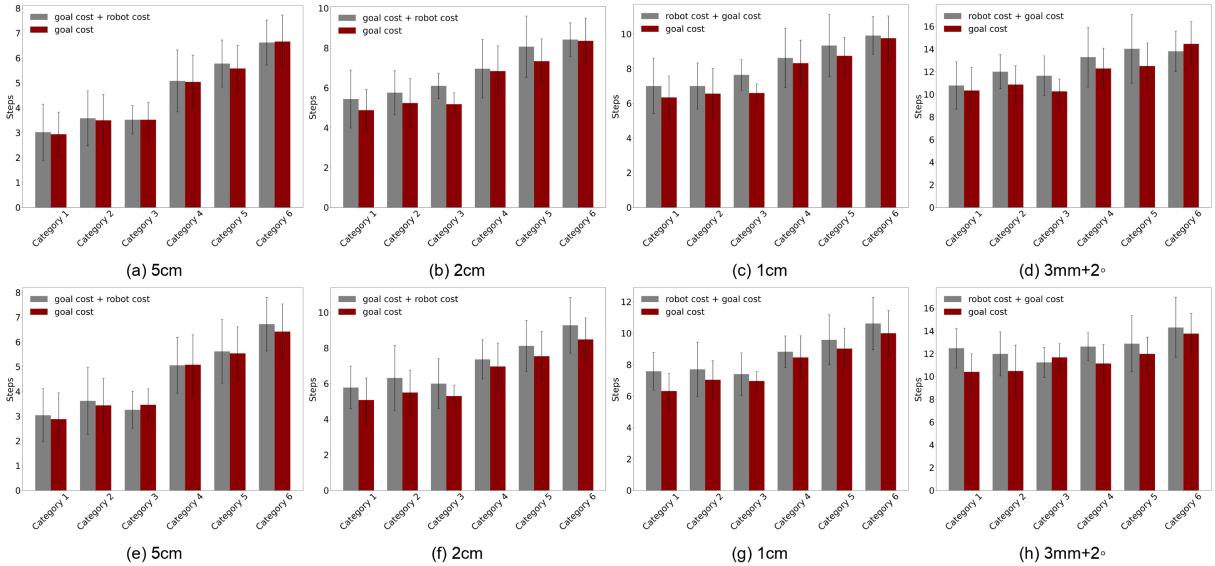


**Fig. 9:** Number of steps taken by the improved method across different categories in long-distance pushing scenarios. Results are evaluated at four success thresholds—5 cm, 2 cm, 1 cm, and 3 mm + 2°—shown from left to right in each group. Each subfigure reports the number of simulation steps required to reach the specified threshold. Rows correspond to different combinations of rollout horizon and initial push direction range: **Row 1** uses Horizon 3 with wide sampling; and **Row 2** uses Horizon 3 with narrow sampling. The horizontal axis in each plot categorizes tasks based on translation distance {10 cm–20 cm, 20 cm–30 cm} and rotation difference {0°–30°, 30°–60°, 60°–90°} between initial and target poses.

## 4.2 Real World

**Real World Setup:** We conduct a series of real-world experiments to evaluate the effectiveness of the basic planar pushing method. The robotic setup consists of a Franka Emika Panda robot, which holds a 15 cm stick equipped with an elastic spherical ball attached to its tip. A Kinect 360 RGBD camera is used to perform markerless tracking of object poses in real time. We use an old sensor without markers to have a challenging noisy environment to provide a sharp contrast to the simulation environment. The experiments were performed on a 90 cm by 60 cm table. The tracking standard deviation was around 1 mm and 1 degrees but some far away parts of the table resulted in systematic errors due to camera angles which we avoid. This setup provides a realistic and challenging evaluation environment and can be seen in Fig. 1. To ensure quasi-static conditions during real-world trials, the robot’s velocity is limited to a maximum of 10 cm/s. Unlike in simulation, where both velocity and step

duration are explicitly defined, the real-world execution uses a simple position controller to push the object according to the selected action. To maintain accurate pose tracking, the robot takes a brief step backward after each action, allowing the perception system to reacquire the object pose before selecting and executing the next action. The speed of our real-world experiments is limited by the backward movement required at each step; however, we have demonstrated that our system operates efficiently and fast enough in simulation.

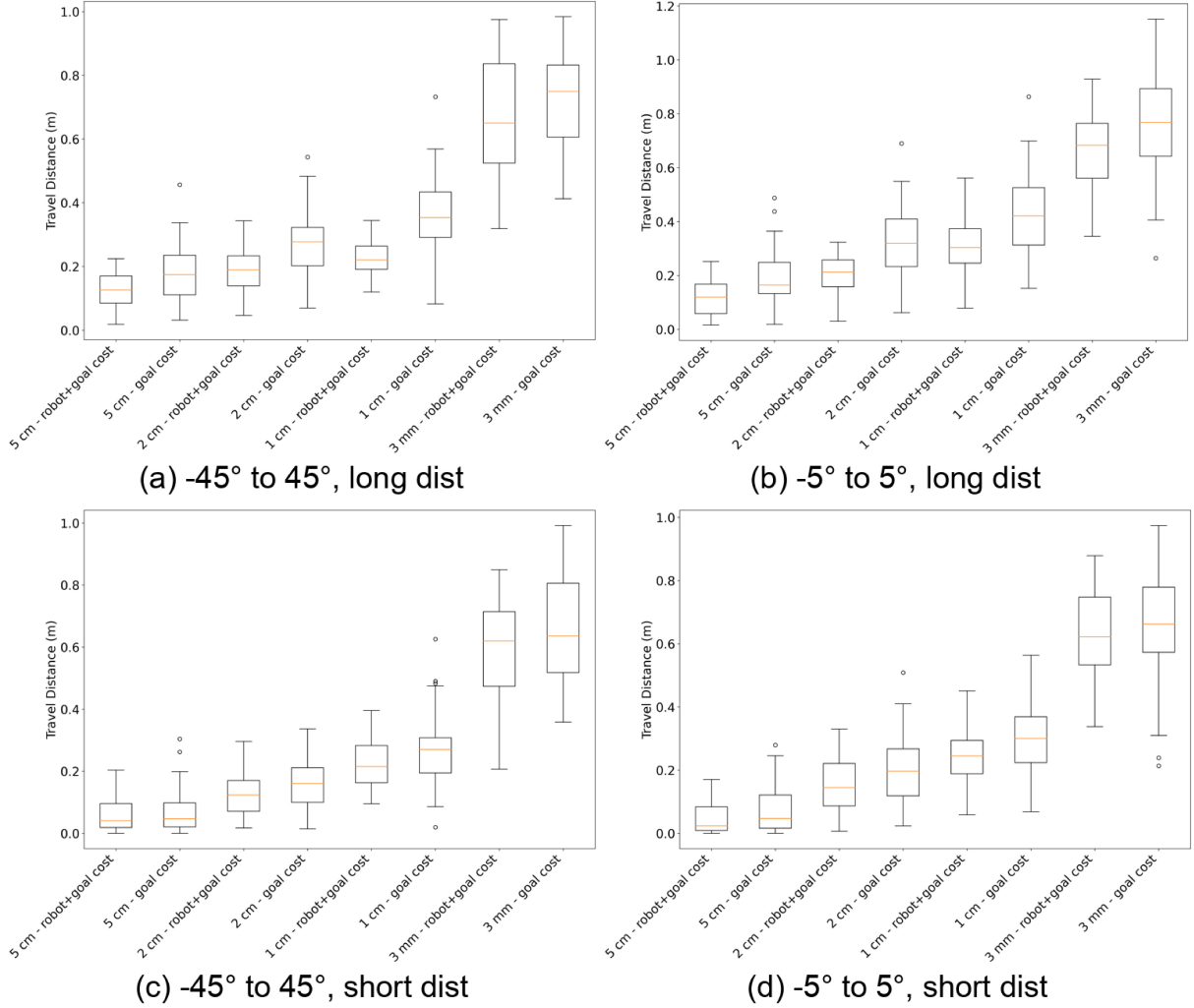


**Fig. 10:** Robot travel distance for the improved version in simulation. Comparison of “goal cost” (Eq. 6) and “robot cost + goal cost” (Eq. 7) across different pushing scenarios. Initial push directions are sampled from either a wide range ( $[-45^\circ, 45^\circ]$ ) in (a), (c) or a narrow range ( $[-5^\circ, 5^\circ]$ ) in (b), (d). Each pair contrasts long vs. short pushing distances and rollout horizons.



**Fig. 14:** The objects used in the real-world experiments. The box at the bottom, object 1, has dimensions of  $9 \times 11$  cm, the box at the top, object 2, has dimensions of  $10 \times 12$  cm, and the box on the right, object 3, has dimensions of  $13 \times 11$  cm.

**Precise Manipulation:** We perform the precise posing task on three objects, shown in Fig. 14. We divide the experiments into two categories: short distances (position: 9-15 cm, orientation:  $0-60^\circ$ ) and long distances (position: 15-20 cm, orientation:  $60-90^\circ$ ), with all objects starting at the same initial pose. We perform a total of 300 push episodes. Additionally, we conduct twenty experiments in which both the initial and target poses are randomly chosen.

Fig. 15 illustrates the number of steps required to reach the target poses. The results mirror that

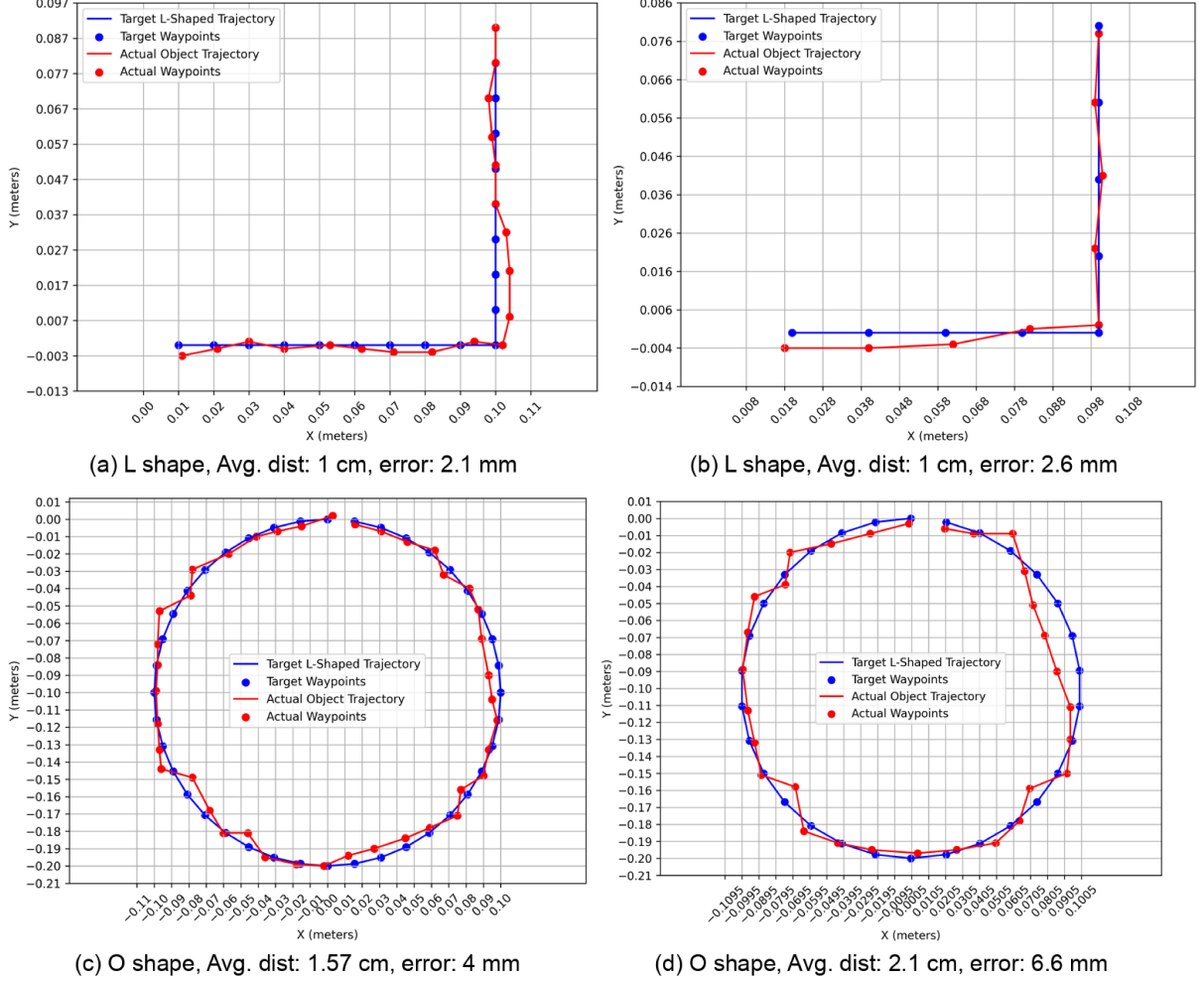


**Fig. 11:** Representative simulation results of trajectory following without orientation cost. Top row: L-shaped trajectories with push sizes of 1 cm and corresponding average position errors of 2.1 mm and 2.6 mm. Bottom row: circular (O-shaped) trajectories with push sizes of 1.57 cm and 2.1 cm, and corresponding average position errors of 4 mm and 6.6 mm. These cases demonstrate the controller’s high accuracy across different path geometries and step sizes.

of the simulation case. In addition, we can see that the required number of steps increase with object size. Table 4 shows the success rate of all the pushes for 1cm position and two a posteriori orientation thresholds. Note that the objective included orientation but the stopping condition did not, which explains less than 100% success rates. The numbers are fairly close for all cases and they are all relatively high. This shows the real-world performance of our approach. We lastly run 10 short distance object 1 cases with a (5 mm,

2°) threshold with average 10.8 steps and 100% success rate.

We also measured the one-step prediction error of the push dynamics model. The average distance error is 3.8 mm for the same starting pose cases and 4.8 mm for the random starting pose cases, while the average orientation error is 2.5° for aforementioned cases.

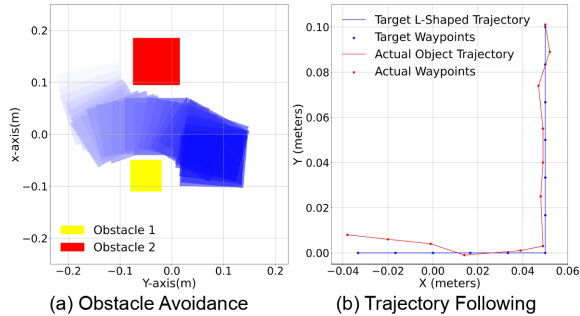


**Fig. 12:** Obstacle avoidance (a) and trajectory following (b) cases in the real world. (a) illustrates a two-obstacle scenario where the object rotates to pass through the narrow passage and then rotates again to reach the target pose. (b) depicts an "L"-shaped trajectory following in a real-world scenario, with a one-step average prediction error of 5.6 mm.

**Table 4:** Success rates for reaching the target pose in manipulation tasks for less than the mentioned thresholds.

Episode Type	5 degrees	10 degrees
Long Distant Episodes	0.875	0.98
Short Distant Episodes	0.86	0.97
Random Episodes	0.9	0.95

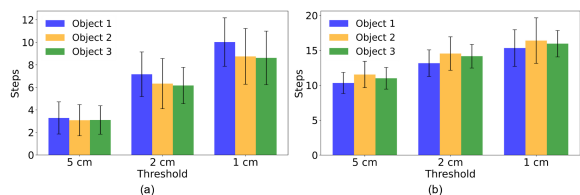


**Fig. 15:** The performance of our method in real-world experiments. The left subfigure correspond to short distance (9-15 cm,  $0^{\circ}$ - $60^{\circ}$ ) configurations and the right subfigure to long distance (15-20 cm,  $60^{\circ}$ - $90^{\circ}$ ) configurations.

**Trajectory Following:** The trajectory following evaluations are conducted with two distinct shapes for the object's path: a circular trajectory and an L-shaped trajectory. In each experiment, the robotic pusher was tasked with guiding the object along these predefined shapes while minimizing the distance between successive waypoints to less than half of the set distances. The average displacement error ranged from 5 to 7 mm, with

the average push length between 1.67 cm and 2 cm for L-shaped trajectories. For circular trajectories, the average displacement error ranged from 6 to 7 mm, with the average push length again between 1.67 cm and 2 cm. Fig. 12b shows an example L-shaped trajectory following result.

**Obstacle Avoidance:** We evaluated the obstacle avoidance task through five experiments with a single obstacle and five experiments with two obstacles. In these tests, our method successfully reached the target pose while avoiding obstacles, maintaining a safe distance of at least 1 cm without any collisions. Fig. 13 illustrates the robot pushing the object to the target pose while avoiding a single obstacle. Fig. 12a shows the object trajectory for a more difficult 2 obstacle case. However, similar to the simulation case and as expected, our method struggles to find a feasible solutions for more complex configurations. The reasons are the same as the simulation case with the added issues of perception noise.

## 5 Discussion

In this work, we proposed a framework that decouples the dynamics model from the controller for planar pushing. A detailed comparison with other methods is not straightforward, since many of them incorporate additional objects and perception-based state representations, making their models inherently aware of object shape and size. In contrast, our model achieved high accuracy: less than 1 mm and  $0.5^{\circ}$  error on a basic dataset, and less than 2 mm and  $2^{\circ}$  error on a more diverse dataset. Considering the variety in pushing lengths and directions, as well as the consistent performance observed in the precision positioning task, these results demonstrate that our model successfully learns the dynamics of cubic object pushes and generalizes to new environments and object sizes with our representation. Moreover, while other model-based approaches without perception cannot exhibit side-switching behavior, our framework enables it through a carefully designed state representation and sampling of orientation and side during control. While prior works such as (Bauza and Rodriguez, 2017; Wang et al., 2024) employ non-parametric methods for learning forward dynamics models, our approach leverages a recurrent neural network to incorporate history encoding and to enable faster

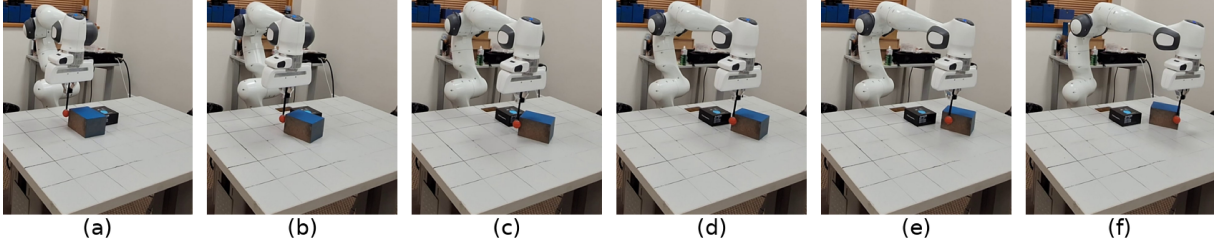


**Fig. 13:** Frames from real-world object avoidance case.

prediction on our large-scale dataset. The proposed model demonstrated improved performance compared to the method presented in (Cong et al., 2020). Specifically, we incorporated additional MLP layers at the final stages of the GRU-based architecture, enabling the model to better capture the non-linear dynamics inherent in pushing interactions. Furthermore, by including the relative pose in our state representation in addition to the push magnitude, we enabled side-switching behavior during execution. Side-switching allows the controller to adaptively change the pushing side and select optimal contact points to guide the object more efficiently toward the target pose. A critical design aspect that enabled this capability was the computation of relative pose and push magnitudes with respect to the object’s current orientation, ensuring consistency and generalization across varying scenarios.

Our extensive experiments demonstrate that the proposed method can achieve high accuracy of sub-centimeter and reaching within 2 cm of the goal pose in under 10 steps, even for long-horizon tasks spanning distances of 20–30 cm. This represents a significant improvement over prior non-prehensile manipulation methods, which typically aimed only to push the object from its initial pose to the target pose without explicitly handling precise intermediate positioning. While our basic method relied on MPPI in its raw form, we improved the framework by extending the push length, incorporating balanced sampling across sides, and introducing greedy action selection. These enhancements effectively reduced the number of steps required to reach the goal and lowered the overall motion planning effort of the robot. Visual and quantitative comparisons between the basic and improved versions clearly show the benefits: the improved framework achieves faster

convergence while balancing position and orientation corrections, particularly in longer-distance tasks where greater positional freedom allows for better orientation adjustments.

Overall, our results highlight significant improvements over previous model-based approaches that do not incorporate perception and, at the same time, demonstrate advantages over model-free methods. Unlike model-free strategies, which often require task-specific training, our learned model can be adapted to multiple tasks simply by modifying the cost function or control objective, without additional retraining. This flexibility underscores the broader potential of combining model-based learning with sampling-based control for robust and versatile non-prehensile manipulation.

## 6 Conclusion and future work

We proposed a novel GRU-based dynamics model for planar pushing, trained in simulation with extensive domain randomization to improve generalization to real-world conditions. Coupled with a sampling-based Model Predictive Path Integral (MPPI) controller, our approach effectively exploits the learned dynamics to generate adaptive, task-oriented actions. By leveraging a state–action representation that encodes both relative pose and push directions, the framework enables versatile capabilities such as object-side switching, variable-length pushes, and integration of diverse objectives. These features collectively allow the system to achieve not only precise positioning but also more complex behaviors such as trajectory following and obstacle avoidance. Through systematic evaluation, we demonstrated the efficacy of our method in both simulated environments and real-world experiments

with a Franka Panda robot equipped with markerless tracking. The results confirmed high success rates in precise positioning tasks under demanding thresholds of position and orientation, while also showing robust performance in dynamic tasks like obstacle avoidance and path following. Building upon this foundation, we also introduced an improved version of our framework designed to address long-horizon tasks more efficiently. Specifically, we trained a model capable of handling longer pushes and incorporated a balanced sampling strategy across object sides. Combined with a greedy action selection mechanism, this enhancement allowed the controller to prioritize high-quality actions, significantly reducing the number of steps required to achieve longer-horizon objectives. This improved framework demonstrated faster convergence toward task goals while maintaining robustness.

Despite these encouraging results, several avenues remain for improvement. Our current controller, although enhanced with balanced sampling, still relies on sampling-based rollouts, which can be computationally demanding. Future work can explore more sophisticated, goal-aware sampling strategies, for example by learning a sampling policy or developing an inverse dynamics model to guide exploration. Additionally, learning a dedicated sampling function could streamline the selection of optimal actions within rollouts, thereby reducing planning time while improving efficiency. These enhancements would allow the framework to scale to more complex environments, enabling it to handle more challenging obstacle-avoidance and long-horizon planning tasks. Another promising direction is to integrate our method with a global planner, allowing the system to seamlessly combine local pushing strategies with long-range planning objectives. Finally, to broaden the applicability of our approach, future efforts should focus on integrating perceptual representations derived from vision-based inputs, which would allow the model to generalize across a wider variety of object geometries.

## References

- Arruda, E., Mathew, M.J., Kopicki, M., Mistry, M., Azad, M., Wyatt, J.L.: Uncertainty
- averse pushing with model predictive path integral control. In: 2017 IEEE-RAS 17th International Conference on Humanoid Robotics (Humanoids), pp. 497–502 (2017). IEEE
- Bauza, M., Alet, F., Lin, Y.-C., Lozano-Pérez, T., Kaelbling, L.P., Isola, P., Rodriguez, A.: Omnipush: accurate, diverse, real-world dataset of pushing dynamics with rgb-d video. In: 2019 IEEE/RSJ International Conference on Intelligent Robots and Systems (IROS), pp. 4265–4272 (2019). IEEE
- Bauza, M., Rodriguez, A.: A probabilistic data-driven model for planar pushing. In: 2017 IEEE International Conference on Robotics and Automation (ICRA), pp. 3008–3015 (2017). IEEE
- Cong, L., Grner, M., Ruppel, P., Liang, H., Hendrich, N., Zhang, J.: Self-adapting recurrent models for object pushing from learning in simulation. In: 2020 IEEE/RSJ International Conference on Intelligent Robots and Systems (IROS), pp. 5304–5310 (2020). IEEE
- Cong, L., Liang, H., Ruppel, P., Shi, Y., Görner, M., Hendrich, N., Zhang, J.: Reinforcement learning with vision-proprioception model for robot planar pushing. *Frontiers in Neuro-robotics* **16** (2022)
- Dengler, N., Ferrandis, J.D.A., Moura, J., Vijayakumar, S., Benezit, M.: Learning goal-directed object pushing in cluttered scenes with location-based attention. arXiv preprint arXiv:2403.17667 (2024)
- Ferrandis, J.D.A., Moura, J., Vijayakumar, S.: Nonprehensile planar manipulation through reinforcement learning with multimodal categorical exploration. In: 2023 International Conference on Intelligent Robots and Systems (IROS), pp. 5606–5613 (2023). IEEE
- Gao, Z., Elibol, A., Chong, N.Y.: Non-prehensile manipulation learning through self-supervision. In: 2020 Fourth IEEE International Conference on Robotic Computing (IRC), pp. 93–99 (2020). <https://doi.org/10.1109/IRC.2020.00022>

- Goyal, S., Ruina, A., Papadopoulos, J.: Limit surface and moment function descriptions of planar sliding. In: 1989 IEEE International Conference on Robotics and Automation, pp. 794–795 (1989). IEEE Computer Society
- Jia, Y.-B., Erdmann, M.: Pose and motion from contact. *The International Journal of Robotics Research* **18**(5), 466–487 (1999) <https://doi.org/10.1177/027836499901800504> <https://doi.org/10.1177/027836499901800504>
- Kingma, D.P., Ba, J.: Adam: A method for stochastic optimization. arXiv preprint arXiv:1412.6980 (2014)
- Kloss, A., Bauza, M., Wu, J., Tenenbaum, J.B., Rodriguez, A., Bohg, J.: Accurate vision-based manipulation through contact reasoning. In: 2020 IEEE International Conference on Robotics and Automation (ICRA), pp. 6738–6744 (2020). IEEE
- Li, J., Lee, W.S., Hsu, D.: Push-net: Deep planar pushing for objects with unknown physical properties. *Robotics: Science and Systems XIV* (2018)
- Lee, G., Lozano-Pérez, T., Kaelbling, L.P.: Hierarchical planning for multi-contact non-prehensile manipulation. In: 2015 IEEE/RSJ International Conference on Intelligent Robots and Systems (IROS), pp. 264–271 (2015). IEEE
- Lynch, K.M.: The mechanics of fine manipulation by pushing. In: Proceedings 1992 IEEE International Conference on Robotics and Automation, pp. 2269–22763 (1992). <https://doi.org/10.1109/ROBOT.1992.219921>
- Mason, M.T.: Mechanics and planning of manipulator pushing operations. *The International Journal of Robotics Research* **5**(3), 53–71 (1986)
- Peng, X.B., Andrychowicz, M., Zaremba, W., Abbeel, P.: Sim-to-real transfer of robotic control with dynamics randomization. In: 2018 IEEE International Conference on Robotics and Automation (ICRA), pp. 3803–3810 (2018). IEEE
- Stüber, J., Zito, C., Stolkin, R.: Let’s push things forward: A survey on robot pushing. *Frontiers in Robotics and AI* **7** (2020) <https://doi.org/10.3389/frobt.2020.00008>
- Tobin, J., Fong, R., Ray, A., Schneider, J., Zaremba, W., Abbeel, P.: Domain randomization for transferring deep neural networks from simulation to the real world. In: 2017 IEEE/RSJ International Conference on Intelligent Robots and Systems (IROS), pp. 23–30 (2017). IEEE
- Williams, G., Drews, P., Goldfain, B., Rehg, J.M., Theodorou, E.A.: Aggressive driving with model predictive path integral control. In: 2016 IEEE International Conference on Robotics and Automation (ICRA), pp. 1433–1440 (2016). <https://doi.org/10.1109/ICRA.2016.7487277>
- Wang, G., Ren, K., Hang, K.: Uno push: Unified nonprehensile object pushing via nonparametric estimation and model predictive control. In: 2024 IEEE/RSJ International Conference on Intelligent Robots and Systems (IROS), pp. 9893–9900 (2024). <https://doi.org/10.1109/IROS58592.2024.10802843>
- Wang, S., Sun, L., Zha, F., Guo, W., Wang, P.: Learning adaptive reaching and pushing skills using contact information. *Frontiers in Neurobotics* **17**, 1271607 (2023)
- Yu, K.-T., Bauza, M., Fazeli, N., Rodriguez, A.: More than a million ways to be pushed. a high-fidelity experimental dataset of planar pushing. In: 2016 IEEE/RSJ International Conference on Intelligent Robots and Systems (IROS), pp. 30–37 (2016). IEEE